nature communications

Article

https://doi.org/10.1038/s41467-024-49981-9

Catalytic properties of trivalent rare-earth oxides with intrinsic surface oxygen vacancy

Received: 10 January 2024

Accepted: 24 June 2024

Published online: 09 July 2024

Check for updates

Kai Xu[1,8], Jin-Cheng Liu[2,3,8], Wei-Wei Wang[1], Lu-Lu Zhou[1], Chao Ma[4], Xuze Guan[5], Feng Ryan Wang[5] ✉, Jun Li[2,6] ✉, Chun-Jiang Jia[1] ✉ & Chun-Hua Yan[7]

Oxygen vacancy (O_v) is an anionic defect widely existed in metal oxide lattice, as exemplified by CeO_2, TiO_2, and ZnO. As O_v can modify the band structure of solid, it improves the physicochemical properties such as the semiconducting performance and catalytic behaviours. We report here a new type of O_v as an intrinsic part of a perfect crystalline surface. Such non-defect O_v stems from the irregular hexagonal sawtooth-shaped structure in the (111) plane of trivalent rare earth oxides (RE_2O_3). The materials with such intrinsic O_v structure exhibit excellent performance in ammonia decomposition reaction with surface Ru active sites. Extremely high H_2 formation rate has been achieved at ~1 wt% of Ru loading over Sm_2O_3, Y_2O_3 and Gd_2O_3 surface, which is 1.5–20 times higher than reported values in the literature. The discovery of intrinsic O_v suggests great potentials of applying RE oxides in heterogeneous catalysis and surface chemistry.

Oxygen vacancy (O_v)[1–3] is a ubiquitous anionic point defect in transition and *f*-element metal oxides. Commonly, the defect type of O_v requires cations with changeable multiple valence states such as $Ce^{3+/4+}$ [4–6] and $Ti^{3+/4+}$ [7,8]. This defect is realized during the treatment in high temperature[9] or reductive conditions[8,10]. The lattice or surface O^{2-} are taken away together with the reduction of metal cations while keeping the crystal structure, leaving O_v within the lattice. On the one hand, the role of O_v in heterogeneous catalysis has been widely reported[4–8]. For example, the generation of O_v in CeO_2 (cubic fluorite structure, $Fm\bar{3}m$ space group) accompanied by the reduction of Ce^{4+} to Ce^{3+} changes its surface charge distribution and creates electrophilic sites[11], which plays a crucial role in improving catalytic performance in CO oxidation, water-gas shift and CO_2 reduction[5,6,9,10]. On the other hand, such redox process is hardly possible with irreducible oxides such as ZrO_2, SiO_2 and Al_2O_3, thereby preventing the generation of defect-based O_v[12–15].

In this work, we discover a new type of surface O_v that does not require a point defect formation nor the redox of metal cations. Such intrinsic O_v stems from the natural atomic arrangements in certain crystalline surface of rare earth oxide (RE_2O_3). We have analysed the structure and surface charge distribution of RE_2O_3 (such as Sm_2O_3, Y_2O_3 and Gd_2O_3) with body-centred cubic structure (*Ia3* space group) based on density functional theory (DFT). An irregular hexagonal sawtooth-shaped structure is found in the (111) surface of those RE_2O_3, forming intrinsic surface O_v. Next to the O_v are penta-coordinated RE^{3+} with strong electrophilic nature. These RE_2O_3 with intrinsic surface O_v are loaded with Ru clusters as active metal (Ru/RE_2O_3, RE = Y, Sm and

[1]Key Laboratory for Colloid and Interface Chemistry, Key Laboratory of Special Aggregated Materials, School of Chemistry and Chemical Engineering, Shandong University, Jinan 250100, China. [2]Department of Chemistry and Engineering Research Center of Advanced Rare-Earth Materials of Ministry of Education, Tsinghua University, Beijing 100084, China. [3]Center for Rare Earth and Inorganic Functional Materials, School of Materials Science and Engineering & National Institute for Advanced Materials, Nankai University, Tianjin 300350, China. [4]College of Materials Science and Engineering, Hunan University, Changsha 410082, China. [5]Department of Chemical Engineering, University College London, Roberts Building, Torrington Place, London WC1E 7JE, UK. [6]Fundamental Science Center of Rare Earths, Ganjiang Innovation Academy, Chinese Academy of Sciences, Ganzhou 341000, China. [7]Beijing National Laboratory for Molecular Sciences, State Key Lab of Rare Earth Materials Chemistry and Applications, PKU-HKU Joint Lab in Rare Earth Materials and Bioinorganic Chemistry, Peking University, Beijing 100871, China. [8]These authors contributed equally: Kai Xu, Jin-Cheng Liu. ✉e-mail: ryan.wang@ucl.ac.uk; junli@mail.tsinghua.edu.cn; jiacj@sdu.edu.cn

Gd) for ammonia decomposition reaction, in which an optimal N-binding strength is required. These Ru/RE_2O_3 catalysts exhibit excellent catalytic performance that is comparable to the most active Ru/CeO_2 catalyst that is equipped with the defect O_v[16], despite that the RE cations are not redox active. During the reaction, the intrinsic O_v has desired absorption strength of NH_3 at the neighbouring RE^{3+}, and causes Ru species more reducible, which facilitates the initial N–H breaking. Such intrinsic O_v shows promise of utilizing their novel properties of RE_2O_3 in catalysis, providing suitable adsorption of reaction molecules for oxidation and hydrogenation chemistry.

Results

Intrinsic O_v in the RE_2O_3 surface

Rare earth oxides with cubic structure, such as Sm_2O_3, Y_2O_3, and Gd_2O_3 mainly expose (111) surface at high temperatures or under harsh reaction conditions[5,17]. We found irregular hexagonal sawtooth-shaped structures formed by three 5-coordinated RE atoms and three 4-coordinated O atoms in cubic-phase Y_2O_3(111), Gd_2O_3(111) and Sm_2O_3(111) (Fig. 1 a–c, e–g, i–k). These vacancy structures are slightly different from the surface point defect O_v in CeO_2(111), which is surrounded by three 6-coordinated Ce (Supplementary Fig. 1). Three RE-O bonds are broken for each oxygen vacancy, and thus 25% outmost oxygen vacancy are missing on the (111) surface. Similar O_v is also observed in Sm_2O_3(110) and (100) surfaces (Supplementary Fig. 2). Due to the exposure of unsaturated 5-coordinated RE atoms, these O_v are electrophilic. Such electrophilic sites can adsorb and activate electron-rich molecules, such as NH_3 and H_2O. The adsorption strength needs to be high enough to form a stable RE-N/O bond and not too high to cause surface poisoning. We have calculated the adsorption energy values of NH_3 molecules on a series of RE_2O_3 and compared with the standard γ-Al_2O_3(111) surface (Supplementary Figs. 3–5 and Supplementary Table 1). The adsorption of NH_3 on the Sm_2O_3(111) surface (−0.44 eV) was stronger than the Sm_2O_3(110) surface (−0.36 eV), but weaker than that on the Sm_2O_3(100) surface (−0.98 eV). The moderate adsorption of NH_3 on Sm_2O_3(111) surface (−0.44 eV) is more favourable to the activation of NH_3 molecule than that on γ-Al_2O_3(111) surface, because the latter exhibits an excessively strong adsorption of NH_3 (−1.74 eV). Besides, in order to illustrate the unique role of intrinsic O_v, which is the special spatial structure in catalysts, the adsorption of molecules at different Sm ions on the surface of Sm_2O_3 is investigated. The adsorption on the vacancy-related Sm sites is stronger than on the non-vacancy Sm sites of Sm_2O_3(111) surface (Supplementary Fig. 6 and Supplementary Table 1), where adsorption might be too weak for effective catalysis. Thus, intrinsic O_v on the Sm_2O_3(111) surface showed great superiority in the adsorption of molecules. Ru is a highly efficient active metal to catalyse the ammonia decomposition reaction[18], so we have constructed a supported catalyst model of Ru_9 clusters on Sm_2O_3(111) surface (Fig. 1d, h, l). The NH_3 adsorption energy on Ru_9/Sm_2O_3(111) is −0.79 eV, indicating that the addition of Ru promotes the adsorption of NH_3 without causing strong binding in Ru_9/Al_2O_3(111) (−1.88 eV). Therefore, RE_2O_3 support metal catalysts can be promising in catalysing reactions involving electron-rich molecules.

Structure and catalytic performance of the Ru/RE_2O_3 catalysts

In order to explore the potential applications of the intrinsic surface O_v in RE_2O_3, a series of Ru/RE_2O_3 (Ru/Sm_2O_3, Ru/Y_2O_3, Ru/Gd_2O_3) and reference Ru/Al_2O_3 catalysts (~1 wt% Ru content, determined by ICP-MS, Supplementary Table 2) were prepared by colloidal deposition

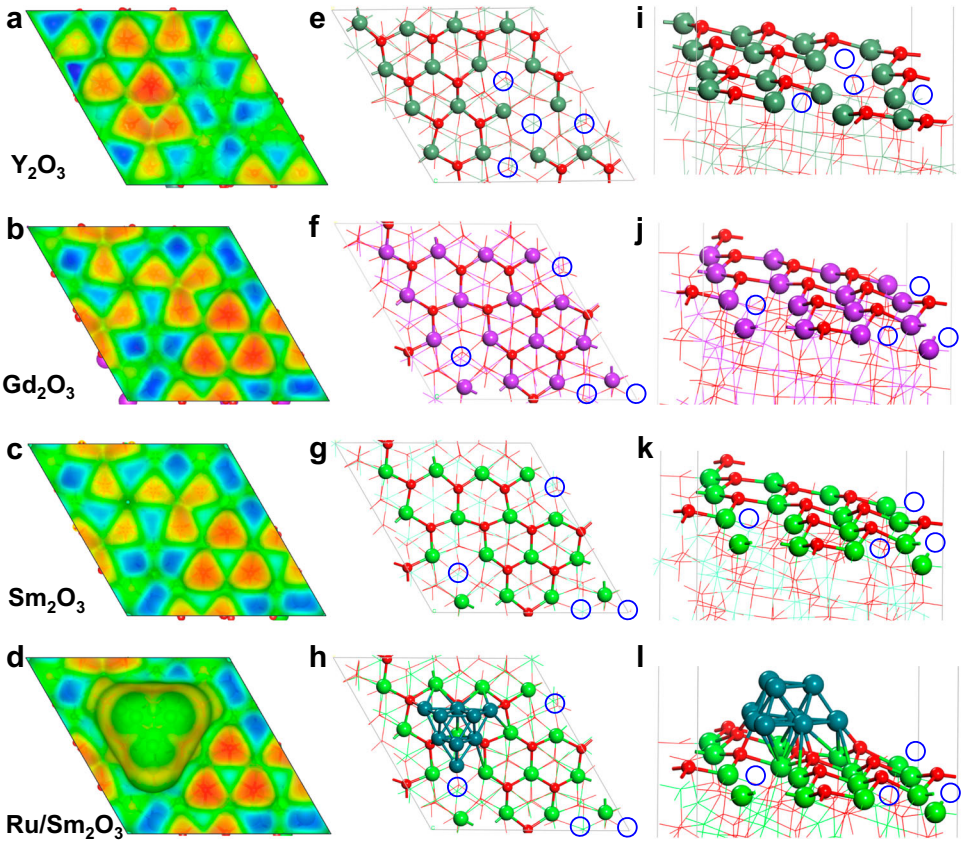

Fig. 1 | Structure and electrostatic potential results of DFT calculations simulating rare earth oxide (111) surfaces. a–d Electron density isosurface mapped with electrostatic potential surface of Y_2O_3(111), Gd_2O_3(111), Sm_2O_3(111), and Ru_9/Sm_2O_3(111), respectively, at 0.003 e·bohr^{-3}; **e–h** top views, and **i–l** side views of optimized surface structure of Y_2O_3(111), Gd_2O_3(111), Sm_2O_3(111), and Ru_9/Sm_2O_3(111), respectively. Blue circles indicate oxygen vacancy or intrinsic surface O_v structures; blue and orange areas on electrostatic potential surface indicate electrophilic and nucleophilic sites, respectively.

https://doi.org/10.1038/s41467-024-49981-9

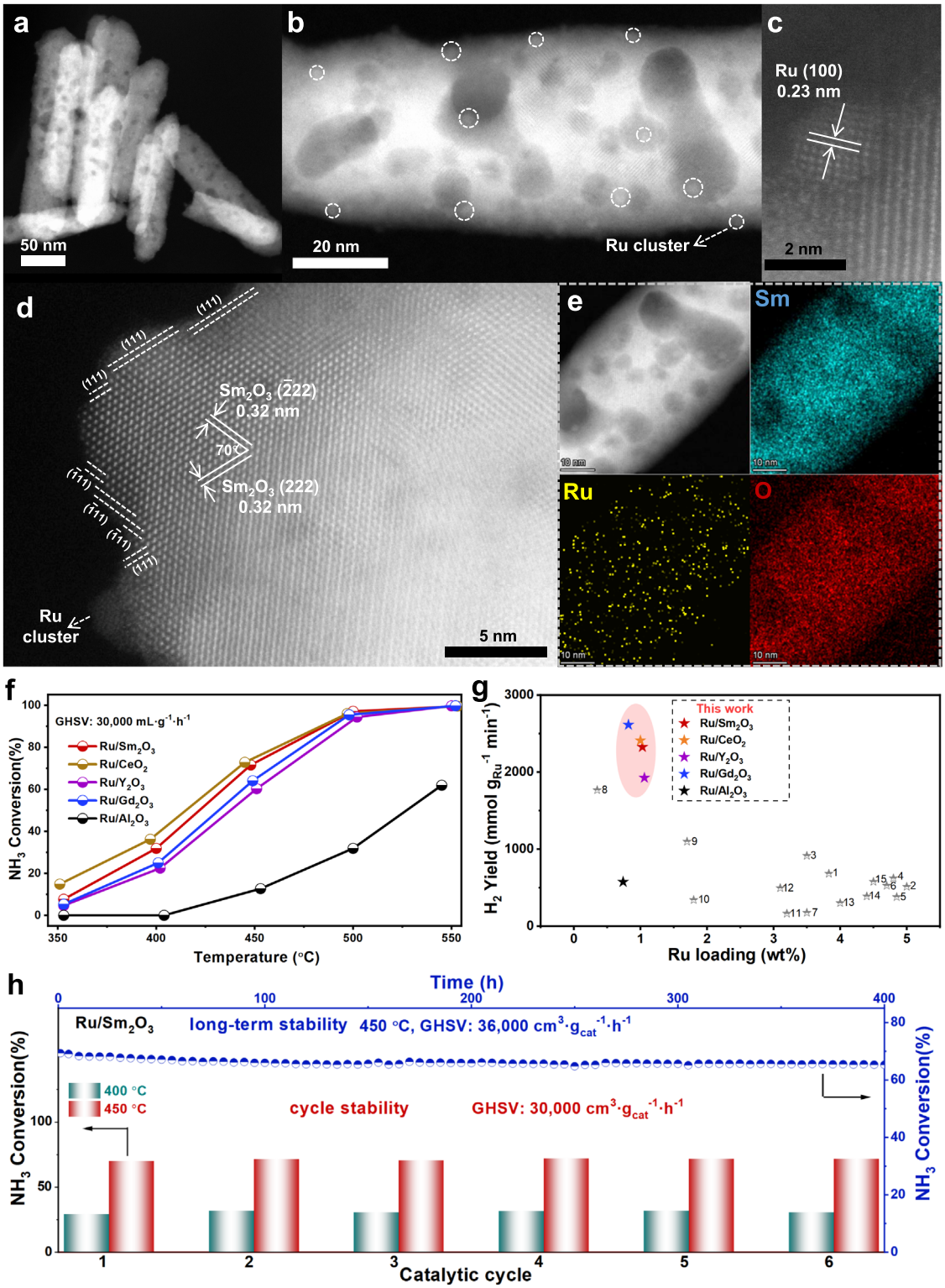

Fig. 2 | The aberration-corrected HAADF-STEM images and catalytic performance test of catalysts. a–d The aberration-corrected HAADF-STEM images of the used Ru/Sm_2O_3; **e** EDS elemental mapping results of the used Ru/Sm_2O_3; **f** temperature-dependent activities of the catalysts (Ru/Sm_2O_3, Ru/Y_2O_3, Ru/Gd_2O_3 and Ru/Al_2O_3, GHSV = 30,000 $mL·g^{-1}·h^{-1}$); **g** comparison of H_2 yield with other Ru-based catalysts: 1: Ru/Sm_2O_3-p[20], 2:Ru/Y_2O_3-p[21], 3: K-Ru/MgO[22], 4: K-Ru/CNTs[23], 5: Ru/MgO-CNTs[24], 6: Ru/c-MgO[25], 7: $Ru/CaAlO_x$-w[26], 8: Ru-Ni/CeO_2[27], 9: Ru/MgO[28], 10: $Ru/LaCeO_x$[29], 11: Ru/CNF[30], 12: Ru-Cs-Mg/MIL-101[31], 13: Ru/Al_2O_3[32], 14: Ru-K/ZrO_2[18], 15: Ru-K/CNT[18]; (h) the long-term stability (GHSV = 36,000 $mL·g^{-1}·h^{-1}$) and the cycle stability test (GHSV = 30,000 $mL·g^{-1}·h^{-1}$) of Ru/Sm_2O_3 catalyst.

method. The transmission electron microscopy (TEM) images of the catalysts were shown in Supplementary Fig. 7. Ru/Sm_2O_3 and Ru/Gd_2O_3 had nanorods structure, while Ru/Y_2O_3 and Ru/Al_2O_3 had nanosheets and nanoparticles morphology, respectively. The high-angle annular dark-field scanning transmission electron microscopy (HAADF-STEM) images showed that the edge of Sm_2O_3 (Fig. 2d and Supplementary Fig. 8), Gd_2O_3 (Supplementary Fig. 9) and Y_2O_3 (Supplementary Fig. 10) supports after the reaction was mostly {111} plane. The high-resolution

transmission electron microscopy (HRTEM) images (Supplementary Fig. 11–14) and the HAADF-STEM images (Fig. 2a–e, Supplementary Figs. 15 and 16) showed the clear presence of very small Ru clusters on the support. In the HAADF-STEM images of Ru/Sm_2O_3 (Fig. 2c) and Ru/Al_2O_3 (Supplementary Fig. 16c, d), we confirmed that the interplanar spacing was consistent with the lattice fringe of Ru (100). According to the particle size distribution (Supplementary Figs. 11c, 12c, 13c, 14c, 17) of all catalysts, the size of Ru cluster in all catalysts was mainly 0.5–2 nm, and the average size was 1.2–1.9 nm. The energy dispersive X-ray spectroscopy (EDS) elemental mappings further confirmed the good dispersion of Ru species on the Sm_2O_3 (Fig. 2e, Supplementary Fig. 15d) and γ-Al_2O_3 (Supplementary Fig. 16e, f). The X-ray diffraction (XRD) patterns (Supplementary Fig. 18) of both the fresh and used catalysts only showed the diffraction peak of the corresponding support, which was consistent with the TEM results because the Ru species were highly dispersed with very low loadings.

The catalytic performances of the Ru-based catalysts (Ru/Sm_2O_3, Ru/Y_2O_3, Ru/Gd_2O_3, Ru/CeO_2 and Ru/Al_2O_3) and corresponding pure oxides materials were evaluated in catalytic ammonia decomposition (Fig. 2f and Supplementary Fig. 19a). This reaction was crucial for online H_2 production using liquid NH_3 as the media for H_2 storage and transportation[19]. First of all, pure metal oxide materials had similar and poor NH_3 conversion, suggesting a non-catalytic process without the presence of Ru. RE_2O_3 supported Ru showed similar activities that were obviously higher than the Ru/Al_2O_3, Ru/TiO_2, Ru/SiO_2 and Ru/CNTs catalyst (Supplementary Fig. 19b). The NH_3 conversion of Ru/RE_2O_3 catalyst at 450 °C was 60–72%, much higher than that of Ru/Al_2O_3 catalyst (only ~13%, GHSV = 30,000 mL·g^{-1}·h^{-1}). The turnover frequency (TOF) value of Ru/Sm_2O_3 (3.2 s^{-1}) was 3 times higher than Ru/Al_2O_3 (1.1 s^{-1}) at 400 °C. The apparent activation energy (E_a, Supplementary Fig. 20) of Ru/Sm_2O_3 (102.2 kJ·mol^{-1}), Ru/Y_2O_3 (123.5 kJ·mol^{-1}) and Ru/Gd_2O_3 (105.1 kJ·mol^{-1}) was lower than that of Ru/Al_2O_3 (136.2 kJ·mol^{-1}), exhibiting superiority in catalytic conversion of NH_3. Interestingly, even though the S_{BET} of Ru/RE_2O_3 (Supplementary Table 2) was only 1/3–1/2 of Ru/CeO_2[16] (S_{BET} = 106 m^2·g^{-1}), Ru/RE_2O_3 catalysts with intrinsic O_v had very similar activity to Ru/CeO_2 with defect-based O_v. It followed that those intrinsic O_v could have similar effects to the defect-based O_v. In addition, the H_2 yield with per Ru species of the Ru/RE_2O_3 catalysts was 1.5–20 times higher than that of other Ru-based catalysts reported[18,20–32] (Supplementary Table 3), proving that the Ru-rare earth oxide catalysts achieved the highest noble-metal atom utilization efficiency for ammonia decomposition reaction at present (Fig. 2g). The durability of Ru/Sm_2O_3 catalyst was evaluated (Fig. 2h). The NH_3 conversion of the Ru/Sm_2O_3 catalyst decayed by only 4% in 400 h test (GHSV = 36,000 mL·g^{-1}·h^{-1}). In addition, after six cycles of stability tests, the catalyst still maintained the same NH_3 conversion at different temperatures (Supplementary Fig. 21), which also verified the excellent stability. We further tested the performance of the Ru/Sm_2O_3 catalyst at lower temperatures by the online mass spectrometer (Supplementary Fig. 22). It was found that the catalyst had started catalysing the reaction at a low temperature as 200 °C and had obvious catalytic activity at 250 °C, showing the extraordinary catalytic performance.

The chemical state of the catalyst surface was explored by X-ray photoelectron spectroscopy (XPS, Fig. 3a–c, Supplementary Figs. 23–25 and Supplementary Table 4), Near Edge X-ray absorption fine structure (NEXAFS) (Supplementary Fig. 26) and the in situ infrared (IR) spectroscopy in the transmission mode (Fig. 3d and Supplementary Fig. 27). The initial catalysts contained mainly cationic Ru for all catalysts. After catalysis, most of the cationic Ru in the Ru/Sm_2O_3 were reduced to metallic Ru, as shown in the XPS result of the used catalyst and the quasi in situ XPS experiment (Fig. 3a). In comparison, after the same treated process, the Ru on Al_2O_3 remained as oxidative state for the used sample (Fig. 3c), only a small amount of Ru was reduced under quasi in situ XPS measurement condition. Such comparison suggested that RE_2O_3 surface with intrinsic O_v helped the reduction of $Ru^{\delta+}$ to Ru^0 in the presence of H_2. In the Sm 3*d* (Fig. 3b) and Y 3*d* (Supplementary Fig. 25b) spectra, Sm^{3+} and Y^{3+} were the only species detected, respectively, confirming their non-reducible nature. The surface properties were studied with the Sm $M_{4,5}$ edges and O *K* edge NEXAFS. Both the fresh and used catalysts had exactly the same Sm^{3+} and O features, suggesting a highly durable surface that maintained the intrinsic O_v (Supplementary Fig. 26). Comparing to the O *K* edge spectrum of bulk O in Sm_2O_3 standard[33], the surface O in the Ru/Sm_2O_3 sample has reduced O 1 s → 5d-π transition comparing to the O 1 s → 5d-σ transition. This showed the slightly different coordination nature between surface and bulk O. To further validate the reduction of Ru, in situ IR experiments during CO adsorption were carried out. The main peak position of Ru/RE_2O_3 was concentrated between 2040 and 2050 cm^{-1}, which was considered as the CO adsorption on Ru^0 species[34,35]. While for Ru/Al_2O_3 catalysts that were concentrated at 2064 cm^{-1}, which was considered as the CO adsorption on $Ru^{\delta+}$ species (Fig. 3d). The temperature-programmed reduction by H_2 (H_2-TPR, Supplementary Figs. 28 and 29) results showed that Ru on RE_2O_3 could be reduced at 123 °C whereas reduction of Ru on Al_2O_3 required 271 °C. Combining XPS, NEXAFS, in situ IR and H_2-TPR, we concluded that Ru over RE_2O_3 with intrinsic O_v preferred Ru^0 whereas Ru over Al_2O_3 remained at Ru^{n+}.

The catalytic function of RE_2O_3 with intrinsic O_v

The combination of XPS, NEXAFS, IR, DRIFTS and H_2-TPR study suggested that Ru over RE_2O_3 could be easily reduced to Ru^0 compared with that of Ru/Al_2O_3. To validate the catalytic function of RE_2O_3 with intrinsic O_v in this process and to the NH_3 decomposition reaction in general, we first used CO_2-temperature programmed desorption (TPD) to investigate the electrophilic nature of the catalyst (Supplementary Fig. 30). Ru/Sm_2O_3 surface contained more medium base sites compared to Ru/Al_2O_3, indicating that Ru/Sm_2O_3 had more effective surface basicity[29]. This medium basicity was conducive to the electron transfer from Sm_2O_3 to Ru species, and further facilitated the dissociative adsorption of N species at Sm^{3+} site. The results of NH_3-TPD (Supplementary Fig. 31) further proved the NH_3 desorption was significantly less than that of Ru/Al_2O_3, which was consistent with the calculation result of adsorption energy values of NH_3 molecules on the surface of catalysts (Supplementary Table 1).

To explore the reaction mechanism, we performed first-principles theoretical calculations (Fig. 4) to further study the N–H dissociation. A Ru (0001) slab was adopted to simulate the large-size Ru nanoparticles while Ru_9 clusters supported on Sm_2O_3(111) slab and γ-Al_2O_3(111) were used to simulate the supported cluster catalyst (Ru/Sm_2O_3 and Ru/Al_2O_3). As shown in Fig. 4a, the N-H bond activation barrier on Ru (0001) surface was 1.16 eV, in good agreement with previous work[36]. Comparatively, the activation barrier of N-H bond on Ru_9/Al_2O_3 and Ru_9/Sm_2O_3 was lowered to 0.76 eV and 0.65 eV, respectively. From Fig. 4b, we could see that on both Ru_9/Sm_2O_3 and Ru_9/Al_2O_3, the N-H dissociation went through a synergistic process that NH_3 adsorbed on the metal cations in the support surface via the formation N-Sm or N-Al interaction. Meanwhile, H atom in NH_3 was captured by the Ru cluster, thus resulting in the N-H bond breaking. So, for Ru_9/Sm_2O_3, the intrinsic O_v sites were responsible for adsorption of NH_3, and the interface Ru atoms played the role of activating N-H bonds. After the first N-H bond break, compared to Ru_9/Sm_2O_3 maintained a relatively active state (−1.85 eV), Ru_9/Al_2O_3 was in a very stable state (−3.31 eV), making it difficult for subsequent reactions to occur. As shown in Fig. 4c, the calculated charge density difference showed that electrons transferred from Sm_2O_3 slab to Ru_9 (Supplementary Fig. 32). This result suggested that Sm_2O_3 was alkalescence and increased the electron density of Ru to dissociate NH_3 more favourably. We further calculated the projected density of states (PDOS) of the Ru_9/Sm_2O_3, isolated NH_3, and Ru (0001) surface (Fig. 4d). To activate the N-H

https://doi.org/10.1038/s41467-024-49981-9

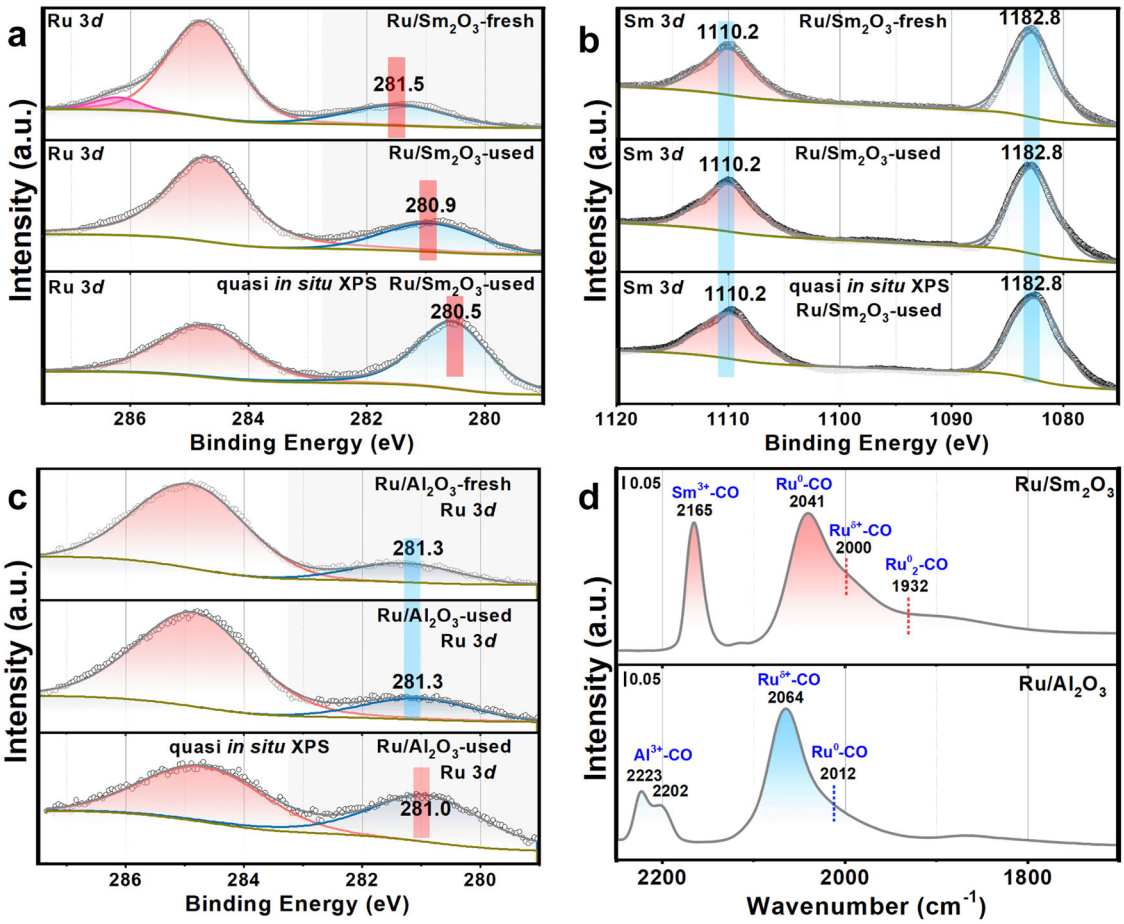

Fig. 3 | Spectroscopy characterization of catalysts. a–**c** XPS results of the fresh and used catalysts: **a** Ru 3*d* of Ru/Sm_2O_3, **b** Sm 3*d* of Ru/Sm_2O_3, **c** Ru 3*d* of Ru/Al_2O_3; **d** the CO adsorption in situ infrared spectroscopy in the transmission mode of used catalysts at 130 K.

bonds, the *d*-band of Ru and LUMO of NH_3 must be at similar energy level, which meant Ru metals with higher *d*-band centre will interact with NH_3 stronger[37]. The *d*-band centres of Ru_9 on Sm_2O_3 and Ru (0001) slab were −1.37 eV and −1.95 eV, respectively, which accounts for the higher activity of Ru/Sm_2O_3. The excellent activity of Ru/Sm_2O_3 was partially from the sintering-resistant property of Sm_2O_3 substrate. The calculated bind energies of Ru_9 with Al_2O_3 and Sm_2O_3 were −9.28 eV and −10.24 eV, respectively. Benefiting from the abundant intrinsic surface O_v sites in Sm_2O_3 surface, Ru clusters were held firmly, thus avoiding the coalescence process and exhibiting solid durability[38,39].

Based on the present results, the effects of the RE_2O_3 with intrinsic surface O_v structure for catalysis could be summarized as the following. Firstly, the RE_2O_3 with intrinsic surface O_v promoted the adsorption and activation of the catalyst on Lewis basic reactant molecules to improve the catalytic performance; secondly, the RE_2O_3 with intrinsic surface O_v enhanced the interaction between the active metals and the rare earth oxide supports, raising the *d* band of Ru and increase the energy of surface adsorbed NH_2. To explore the generality of this effect, we prepared Cu/RE_2O_3 and Cu/Al_2O_3 catalysts and tested the activity of the water-gas shift (WGS) reaction (Supplementary Fig. 33), which was also crucial in industrial hydrogen production. The activity of Cu/RE_2O_3 has been found to be significantly higher than that of Cu/Al_2O_3, possibly due to the activation of H_2O and O-H cleavage via intrinsic O_v.

Discussion

In summary, we have discovered a new type of O_v on the surface of RE_2O_3. Those O_v stem from the surface symmetric and the atomic arranges and therefore intrinsic of a crystalline, which is completely different from the conventional defect-based O_v. Such RE_2O_3 with intrinsic O_v is found to play an important role in catalysis, such as ammonia decomposition and WGS reaction. The RE_2O_3 offers significant advantages, including: (1) moderate adsorption of reaction molecules such as NH_3 and H_2O; (2) maintaining active species in metallic state, (3) forming unique RE-N(O)-H-Ru configurations for the N(O)-H bond breaking. Such O_v -metal synergy is new for those redox inactive metal oxide supports and will bring RE_2O_3 on the screening system for heterogenous catalysis.

Methods

Synthesis of catalysts

The typical synthetic method of Ru colloidal solution has been reported previously[16]. Dissolving 0.15 g $RuCl_3$ (Sinopharm) in 50 mL ethylene glycol ($C_2H_6O_2$; Sinopharm), and then added 0.16 g NaOH (Sinopharm) to the mixture with constant stirring for 30 min. Next, the solution was refluxed at 160 °C for 3 h. After cooling to room temperature, we obtained the Ru colloidal solution with dark brown.

Sm_2O_3 nanorod (Sm_2O_3) and CeO_2 nanorod (CeO_2) follow the same hydrothermal method. Dissolving NaOH (14.40 g; Sinopharm) in 40 mL deionized water, and then the solution of 3 mmol nitrate ($Sm(NO_3)_3{\cdot}6H_2O$ (aladdin) and $Ce(NO_3)_3{\cdot}6H_2O$ (kermel)) was added into the previous mixture and kept stirring for 30 min. Then we transferred the solution to the teflon bottle for hydrothermal reaction at 100 °C for 24 h. The precipitate produced was washed and dried overnight at 60 °C to obtain $Sm(OH)_3$ and CeO_2. The $Sm(OH)_3$ was calcined in air at 450 °C for 4 h to obtain Sm_2O_3.

https://doi.org/10.1038/s41467-024-49981-9

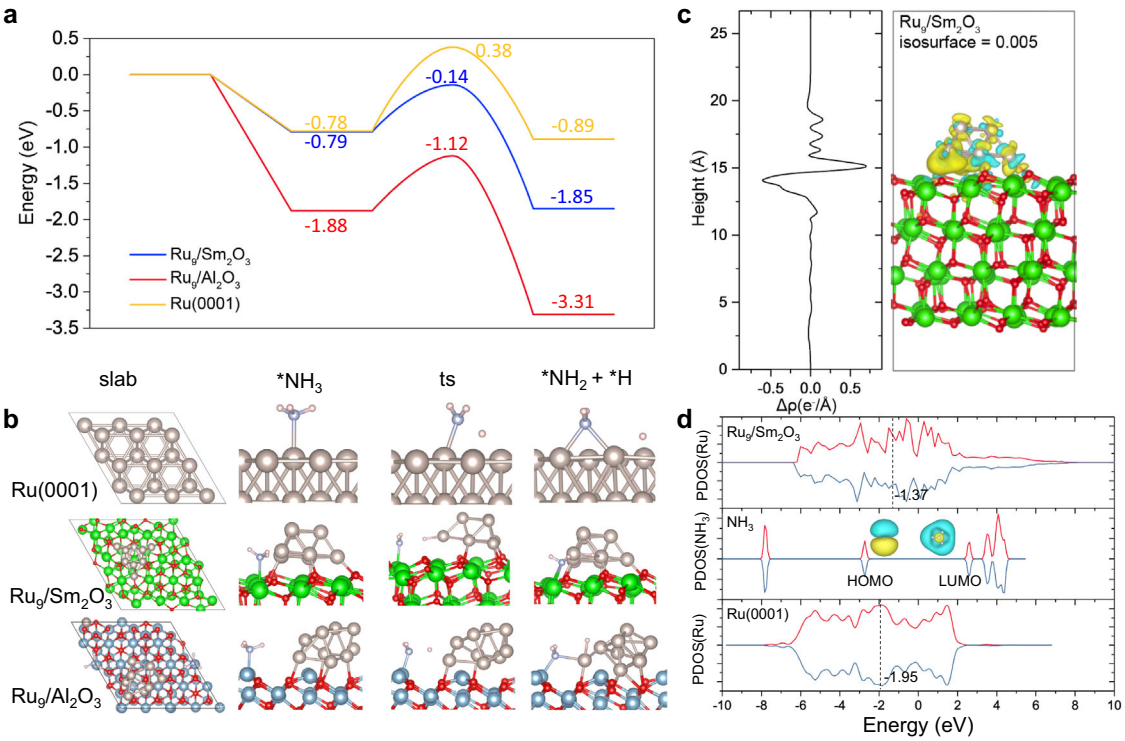

Fig. 4 | Theoretical results for the reaction mechanism and electronic nature of the active sites. a Energy profiles and **b** corresponding structures for NH_3 adsorption and activation of N–H bond on Ru(0001), $Ru_9/Sm_2O_3(111)$, and $Ru_9/Al_2O_3(111)$, respectively; **c** charge density differences, $\Delta\rho = \rho(Ru_9/Sm_2O_3) - \rho(Ru_9) - \rho(Sm_2O_3)$, for Ru_9 adsorption on $Sm_2O_3(111)$ surface (yellow and blue isosurfaces denote where electronic density increase and decrease, respectively) and integration of Δρ in planes parallel to the surface and plotted as a function of the z coordination; (d) the projected density of states (PDOS) of the Ru_9 on Ru_9/Sm_2O_3, isolated NH_3, and Ru(0001) surface (black dash lines label the *d*-band centre of Ru).

Y_2O_3 nanosheet was synthesized by hydrothermal method. Dissolving 1.149 g $Y(NO_3)_3{\cdot}6H_2O$ (aladdin) in 60 mL deionized water. And then using 10% NaOH solution adjusted the pH to 12. Then we transferred the solution to the teflon bottle for hydrothermal reaction at 120 °C for 12 h. The precipitate produced was washed and dried overnight at 60 °C. Finally, it was calcined in the air at 500 °C for 6 h.

Gd_2O_3 nanorod was synthesized by hydrothermal method. Dissolving 0.02 mol $Gd(NO_3)_3{\cdot}6H_2O$ (aladdin) in 50 mL deionized water. And then using 2.5 mol·L^{-1} NaOH solution adjusted the pH to 12.8. Then we transferred the solution to the teflon bottle for hydrothermal reaction at 180 °C for 24 h. The precipitate produced was washed and dried overnight at 80 °C. Finally, it was calcined in the air at 450 °C for 2 h.

The Ru-based catalysts were synthesized according to the previous methods[16]. The typical steps of colloidal deposition method were shown as followed. 1 g supports (Sm_2O_3, CeO_2, Y_2O_3, Gd_2O_3 and γ-Al_2O_3 (commercial, Macklin)) was dissolved and dispersed in 25 mL deionized water, and then added a certain amount of Ru colloid to this mixture and kept stirring for 48 h. Next, ageing for 12 h and the precipitates were collected and washed by centrifugation. The obtained products were dried for 48 h at 60 °C. Finally, the catalysts were reduced in NH_3 atmosphere at 550 °C before catalytic test.

Characterization of catalysts

The inductively coupled plasma mass spectrometer (ICP-MS, PerkinElmer, NexION 350X) analysis was used to detect the actual content of Ru. The N_2 adsorption–desorption measurements were on a Builder SSA-4200 analyzer at −196 °C. All the samples were pretreated at 200 °C for 400 min under vacuum. The BET (according to the Brunauer, Emmett and Teeler method) specific surface area (S_{BET}) can be calculated from that. The X-ray diffraction (XRD) was carried out on a PANalytical X'pert3 powder diffractometer (40 kV, 40 mA) using Cu Kα radiation (λ = 0.15406 nm). The diffraction angles (2θ) ranged from 10° to 90°. The thermogravimetric analysis (TGA) was carried out on a simultaneous thermal analyzer (METTLER, TGA/DSC3 +) in N_2. The transmission electron microscopy (TEM) images were conducted on a JEOL JEM-2100F microscope operating at 100 kV. The high-resolution TEM (HRTEM) was carried out under 200 kV on a FEI Talos F200s microscope. The high-angle annular dark-field scanning transmission electron microscopy (HAADF-STEM) images were obtained on a JEOL ARM200F microscope equipped with a probe-forming spherical-aberration corrector and Gatan image filter (Quantum 965). The hydrogen temperature-programmed reduction (H_2-TPR) measurements were carried on a Builder PCSA-1000 instrument. After pretreated at 500 °C in air, 50 mg catalysts were reduced by 5%H_2/Ar (30 mL·min^{-1}) from room temperature to 700 °C. The H_2 consumption was shown by the thermal conductivity detector (TCD). The X-ray photoelectron spectroscopy (XPS) measurements were carried out on an Thermo scientific ESCALAB Xi^+ XPS spectrometer with Al Kα radiations, and with the C 1*s* peak at 284.8 eV as an internal standard for all the spectra. The in situ infrared spectroscopy in the transmission mode measurements were conducted in a UHV apparatus combining a FTIR spectrometer (Bruker Vertex 70 v) with a multi-chamber UHV system. The sample was pretreated with H_2 in a vacuum at 873 K for 30 min, and then exposed to CO (10^{-2} mbar) at 130 K to collect the spectrogram.

Near Edge X-ray absorption fine structure (NEXAFS) experiments were carried out at the VerSoX beamline (B07-C) of Diamond Light Source (DLS, UK). The beamline has a maximum resolving power hv/Δ(hv) > 5000 with a photon flux > 10^{10} photons s^{-1} from 170 eV to 2000 eV and can be operated (delivering lower flux) up to 2800 eV. The accuracy of the sample and analyser position is typically less than 10 μm. The gas pressure and composition are controlled via a butterfly valve and mass flow controllers. The endstation consists of a fixed

interface flange which holds the entrance cone of the ambient-pressure electron energy analyser (SPECS Phoibos NAP-150). The samples (around 1 mg) were dispersed in water (around 1 mL) and dropped (around 2 droplets) on Au-coated Si (~1 cm × 1 cm), followed by heating at 70 °C to remove the solvent. NEXAFS spectra at Sm M_4/M_5 edge and O K-edge were measured in both total electron yield (TEY) mode and Auger electron yield (AEY) mode at room temperature. The measurements were performed under UHV condition.

The temperature programmed desorption (TPD) measurements of the catalysts were performed at the online mass spectrometer (TILON LC-D200M). For the typical NH_3-TPD experiments, 300 mg catalysts (20–40 mesh) were pretreated at 550 °C for 1 h in NH_3 atmosphere (20 mL·min^{-1}). And then it was cooled to room temperature, and held for 1 h in the NH_3 atmosphere. Next, switched to Ar and purged until the baseline was stable, collected the signal from room temperature to 800 °C. For the typical CO_2-TPD experiments, 300 mg catalysts (20–40 mesh) were pretreated at 550 °C for 1 h in 5%H_2/Ar (30 mL·min^{-1}). And then it was cooled to room temperature, and held for 1 h in the CO_2 atmosphere. Next, switched to Ar and purged until the baseline was stable, collected the signal from room temperature to 800 °C. For the reaction at lower temperatures, 50 mg catalysts (20–40 mesh) were pretreated at 550 °C for 1 h in NH_3 atmosphere (20 mL·min^{-1}). After cooling down, we collected the signal from 100 °C to 300 °C with a step of 50 °C in continuous pure NH_3 flow.

Theoretical methods and computational details

All static calculations were carried out using spin-polarized density functional theory (DFT) with generalized gradient approximation (GGA) of Perdew–Burke–Ernzerhof (PBE) and PAW pseudopotentials as implemented in VASP 5.4.4 code[40,41]. DFT + U method with U = 4 eV was used to describe the localized rare earth 4*f* states[42]. The valence orbitals were described by plane-wave basis sets with a cutoff energy of 400 eV. Considering the large size of p(4×4)-(111) slabs used in this work, the single gamma-point grid sampling was used for Brillouin Zone integration for geometry optimization, and 3 × 3 × 1 k-mesh was used for density of states calculations. Atomic positions were optimized by using the conjugate gradient algorithm until the forces were less than 0.03 eV/Å. Transition states were searched by climbing image nudged-elastic-band (CI-NEB) method with convergence criterion of 0.05 eV/Å[43,44]. The criterion for electronic self-consistent field convergence was set to 10^{-6} eV.

Catalytic tests

The catalytic performance of the catalysts was tested in a self-constructed fixed-bed flow reactor. The temperature controller (UDIAN, XIAMEN YUDIAN AUTOMATION TECHNOLOGY CO., LTD.) was used in the reactor temperature control system. During the test, 50 mg catalysts (20–40 mesh) mixed with 500 mg quartz sand (20–40 mesh) and then packed into the reactor with an inner diameter of 6 mm. Before the test, the catalysts were activated at 550 °C in pure NH_3 atmosphere. Then the activity test was performed from 350 to 550 °C with a step of 50 °C for the reactor temperature (GHSV = 30,000 mL·g^{-1}·h^{-1}). The outlet gas was analyzed by an online gas chromato-graph (Ouhua GC 9160), and then the real-time N_2 and NH_3 contents were obtained. The NH_3 conversion was calculated through Eq. (1).

$$X_{NH_3} = \frac{2 \times n_{N_2}^{out}}{2 \times n_{N_2}^{out} + n_{NH_3}^{out}} \times 100\% \quad (1)$$

The stability test of the catalysts was conducted at 450 °C (GHSV = 36,000 mL·g^{-1}·h^{-1}) for 400 h. The apparent activation energy for the reaction was determined with an equal conversion of 12.5% by tuning the flow rate and temperature.

Data availability

The main data supporting the findings of this study are available within the article and its Supplementary Information. Additional data are available from the corresponding authors upon request. Source data are provided with this paper.

References

1. TOMPKINS, F. C. Superficial chemistry and solid imperfections. *Nature* **186**, 3–6 (1960).
2. Xie, C. et al. Defect chemistry in heterogeneous catalysis: recognition, understanding, and utilization. *ACS Catal.* **10**, 11082–11098 (2020).
3. Wang, G. et al. Oxygen defective metal oxides for energy conversion and storage. *Nano Today* **13**, 23–39 (2017).
4. Campbell, C. T. & Peden, C. H. F. Oxygen vacancies and catalysis on ceria surfaces. *Science* **309**, 713 (2005).
5. Zhang, Y. et al. Unraveling the physical chemistry and materials science of CeO_2-based nanostructures. *Chem* **7**, 2022–2059 (2021).
6. Kang, L. et al. Adsorption and activation of molecular oxygen over atomic copper(I/II) site on ceria. *Nat. Commun.* **11**, 4008 (2020).
7. Schaub, R. et al. Oxygen-mediated diffusion of oxygen vacancies on the TiO_2(110) surface. *Science* **299**, 377–379 (2003).
8. Xu, M. et al. Insights into interfacial synergistic catalysis over Ni@TiO_{2-x} catalyst toward water–gas shift reaction. *J. Am. Chem. Soc.* **140**, 11241–11251 (2018).
9. Yu, W.-Z. et al. Construction of active site in a sintered copper–ceria nanorod catalyst. *J. Am. Chem. Soc.* **141**, 17548–17557 (2019).
10. Yan, H. et al. Construction of stabilized bulk-nano interfaces for highly promoted inverse CeO_2/Cu catalyst. *Nat. Commun.* **10**, 3470 (2019).
11. Li, H.-Y. et al. Multiple configurations of the two excess 4*f* electrons on defective CeO_2(111): Origin and implications. *Phys. Rev. B* **79**, 193401 (2009).
12. Bahmanpour, A. M. et al. Cu–Al spinel as a highly active and stable catalyst for the reverse water gas shift reaction. *ACS Catal.* **9**, 6243–6251 (2019).
13. Fan, R. et al. Synergistic catalysis of cluster and atomic copper induced by copper-silica interface in transfer-hydrogenation. *Nano Res.* **14**, 4601–4609 (2021).
14. Li, Y. et al. Selective light absorber-assisted single nickel atom catalysts for ambient sunlight-driven CO_2 methanation. *Nat. Commun.* **10**, 2359 (2019).
15. Feng, J. et al. Applications of rare earth oxides in catalytic ammonia synthesis and decomposition. *Catal. Sci. Technol.* **11**, 6330–6343 (2021).
16. Hu, X.-C. et al. Ceria-supported ruthenium clusters transforming from isolated single atoms for hydrogen production via decomposition of ammonia. *Appl. Catal. B. Environ.* **268**, 118424 (2020).
17. Nolan, M. et al. Density functional theory studies of the structure and electronic structure of pure and defective low index surfaces of ceria. *Surf. Sci.* **576**, 217–229 (2005).
18. Yin, S. et al. Investigation on the catalysis of CO_x-free hydrogen generation from ammonia. *J. Catal.* **224**, 384–396 (2004).
19. Lucentini, I. et al. Review of the decomposition of ammonia to generate hydrogen. *Ind. Eng. Chem. Res.* **60**, 18560–18611 (2021).
20. Zhang, X. et al. Metal–support interaction-modulated catalytic activity of Ru nanoparticles on Sm_2O_3 for efficient ammonia decomposition. *Catal. Sci. Technol.* **11**, 2915–2923 (2021).
21. Feng, J. et al. Highly dispersed ruthenium nanoparticles on Y_2O_3 as superior catalyst for ammonia decomposition. *ChemCatChem* **13**, 1552–1558 (2021).
22. Ju, X. et al. Mesoporous Ru/MgO prepared by a deposition-precipitation method as highly active catalyst for producing CO_x-free hydrogen from ammonia decomposition. *Appl. Catal. B. Environ.* **211**, 167–175 (2017).

23. Yin, S. F. et al. Carbon nanotubes-supported Ru catalyst for the generation of CO_x-free hydrogen from ammonia. *Catal. Today* **93–95**, 27–38 (2004).
24. Yin, S. F. et al. Magnesia–carbon nanotubes (MgO–CNTs) nanocomposite: novel support of Ru catalyst for the generation of CO_x-free hydrogen from ammonia. *Catal. Lett.* **96**, 113–116 (2004).
25. Ju, X. et al. Highly efficient Ru/MgO catalyst with surface-enriched basic sites for production of hydrogen from ammonia decomposition. *ChemCatChem* **11**, 4161–4170 (2019).
26. Zhao, J. et al. Metal–support interactions on Ru/$CaAlO_x$ catalysts derived from structural reconstruction of Ca–Al layered double hydroxides for ammonia decomposition. *Chem. Commun.* **55**, 14410 (2019).
27. Lucentini, I. et al. Catalytic ammonia decomposition over Ni-Ru supported on CeO_2 for hydrogen production: Effect of metal loading and kinetic analysis. *Appl. Catal. B. Environ.* **286**, 119896 (2021).
28. Hu, X. et al. Hydrogen production via catalytic decomposition of NH_3 using promoted MgO-supported ruthenium catalysts. *Sci. China Chem.* **62**, 1625–1633 (2019).
29. Le, T. A. et al. Ru-supported lanthania-ceria composite as an efficient catalyst for CO_x-free H_2 production from ammonia decomposition. *Appl. Catal. B. Environ.* **285**, 119831 (2021).
30. Duan, X. et al. Carbon nanofiber-supported Ru catalysts for hydrogen evolution by ammonia decomposition. *Chin. J. Catal.* **31**, 979–986 (2010).
31. Li, J. et al. Sub-nm ruthenium cluster as an efficient and robust catalyst for decomposition and synthesis of ammonia: Break the "size shackles". *Nano Res.* **11**, 4774–4785 (2018).
32. Karim, A. M. et al. Correlating particle size and shape of supported Ru/γ-Al_2O_3Catalysts with NH_3 decomposition activity. *J. Am. Chem. Soc.* **131**, 12230–12239 (2009).
33. ltman, A. B. et al. Evidence for 5d-σ and 5d-π covalency in lanthanide sesquioxides from oxygen K-edge X-ray absorption spectroscopy. *Dalton Trans.* **45**, 9948–9961 (2016).
34. Hadjiivanov, K. et al. FTIR study of CO interaction with Ru/TiO_2 catalysts. *J. Catal.* **176**, 415–425 (1998).
35. Chin, S. Y., Williams, C. T. & Amiridis, M. D. FTIR studies of CO adsorption on Al_2O_3- and SiO_2- supported Ru catalysts. *J. Phys. Chem. B.* **110**, 871–882 (2006).
36. Honkala, K. et al. Ammonia synthesis from first-principles calculations. *Science* **307**, 555–558 (2005).
37. Hammer, B. & Nørskov, J. K. Why gold is the noblest of all the metals. *Nature* **376**, 238–240 (1995).
38. Curto, A. G. et al. Unidirectional emission of a quantum dot coupled to a nanoantenna. *Science* **329**, 930–933 (2010).
39. Hu, S. & Li, W. X. Sabatier principle of metal-support interaction for design of ultrastable metal nanocatalysts. *Science* **374**, 1360–1365 (2021).
40. Kresse, G. & Furthmüller, J. Efficiency of ab-initio total energy calculations for metals and semiconductors using a plane-wave basis set. *Comput. Mater. Sci.* **6**, 15–50 (1996).
41. Kresse, G. & Furthmüller, J. Efficient iterative schemes for ab initio totalenergy calculations using a plane-wave basis set. *Phys. Rev. B* **54**, 11169–11186 (1996).
42. Capdevila-Cortada, M., Łodziana, Z. & López, N. Performance of DFT +U approaches in the study of catalytic materials. *ACS Catal.* **6**, 8370–8379 (2016).
43. Mills, G., Jonsson, H. & Schenter, G. K. Schenter, Reversible work transition state theory: application to dissociative adsorption of hydrogen. *Surf. Sci.* **324**, 305–337 (1995).
44. Henkelman, G., Uberuaga, B. P. & Jónsson, H. A climbing image nudged elastic band method for finding saddle points and minimum energy paths. *J. Chem. Phys.* **113**, 9901–9904 (2000).

Acknowledgements

This work was financially supported by National Key Research and Development Program of China (2021YFA1501103), the National Science Fund for Distinguished Young Scholars of China (22225110), the National Science Foundation of China (nos. 22075166, 22271177 and 22033005), the National Science Foundation of Shandong Province of China (ZR2023ZD21 and ZR2023QB187), the Young Scholars Program of Shandong University, EPSRC (EP/P02467X/1 and EP/S018204/2), Royal Society (RG160661, IES\R3\170097, IES\R1\191035, IEC\R3\193038), and by the Guangdong Provincial Key Laboratory of Catalysis (No. 2020B121201002). We thank the Center of Structural Characterizations and Property Measurements at Shandong University for the help on sample characterizations. The calculations were performed by using supercomputers at SUSTech, Tsinghua National Laboratory for Information Science and Technology, and the Computational Chemistry Laboratory of the Department of Chemistry under the Tsinghua Xuetang Talents Program.

Author contributions

C.-J. J., F. R. W., J. L. and C.-H. Y. supervised the work; K. X., L.-L. Z. and C.-J. J. designed the experiments, analyzed the results. K. X., J.-C. L., C.-J. J., F. R. W. and J. L. co-wrote the manuscript; K. X. and W.-W. W. performed the in situ DRIFTS and quasi in situ XPS; J.-C. L. and J. L. performed the DFT calculations and analysed the theoretical data; K. X. performed the catalysts preparation, catalytic tests and the TPR tests; C. M. performed the aberration-corrected HAADF-STEM measurements and analysed the results. X. G. and F. R. W. performed the XAFS experiments and analysed the data.

Competing interests

The authors declare no competing interests.

Additional information

Supplementary information The online version contains supplementary material available at https://doi.org/10.1038/s41467-024-49981-9.

Correspondence and requests for materials should be addressed to Feng Ryan Wang, Jun Li or Chun-Jiang Jia.

Peer review information *Nature Communications* thanks the anonymous reviewer(s) for their contribution to the peer review of this work. A peer review file is available.